The Vibrational Resonance Raman Spectra and the Valence Force Field of Iridium Dichalcogenides, IrS$_2$ and IrSe$_2$

C. SOURISSEAU,* R. CAVAGNAT, AND M. FOUASSIER

Laboratoire de Spectroscopie Moléculaire et Cristalline, U.R.A.124 CNRS, Université de Bordeaux I, 33405 Talence Cedex, France

AND S. JOBIC, P. DENIARD, R. BREC, AND J. ROUXEL

Institut de Physique et Chimie des Matériaux, U.M. 110 CNRS, Université de Nantes, 2, Rue de la Houssinière, 44072 Nantes Cedex, France

The electronic (900–300 nm), infrared, and Raman (500–10 cm^{-1}) spectra of polycrystalline samples of IrS$_2$ and IrSe$_2$ were investigated. A complete vibrational assignment is proposed in terms of stretching and bending motions of IrX$_3$ or IrX$_6$ distorted units and based upon frequency shifts when substituting sulfur by selenium. All the assignments were checked by a complete valence force field calculation of the IrS$_2$ phase, including short-range and long-range interactions where most of the force constants were transferred from the FeS$_2$ pyrite and marcasite compounds. Values of the force constants, of the principal potential energy distributions and mean square vibrational amplitudes definitely confirm the existence of anomalously long (S$_2$) pairs, whose Raman stretching modes appear at 334 and 316 cm^{-1}, and of large constraints beween the various IrS$_6$ units. In addition, a resonance Raman study has been performed using various exciting radiations in the visible region (676.4–457.9 nm) and the Raman excitation profiles of many modes have been obtained. All profiles of totally symmetric modes as well as non-totally symmetric vibrations show intensity enhancement at low energy (in the near-infrared) electronic bands, so that comlex interference and vibronic coupling mechanisms occur: this suggests large overlap of the metal d (Ir) and ligand $p(X)$ type orbitals in the electronic band structures of the very narrow-band semiconducting IrS$_2$ and IrSe$_2$ phases.   © 1991 Academic Press, Inc.

Introduction

The development of high power cells using transition metal dichalcogenides MX_2 (X = S, Se) as cathode materials in ambient temperature lithium secondary batteries is still a problem of current interest. The chalcogenide compounds containing group IVb, Vb, and VIb elements (with the exception of

manganese) occur as two-dimensional (2D) structures and, in contrast, those containing metals on the right of the Periodic Table occur mostly as tridimensional (3D) arrangements of the pyrite or marcasite type. However, in this last family there are several noticeable exceptions; in particular, the IrX_2 and RhSe$_2$ phases display a 3D structural arrangement, as does a new type of FeS$_2$ recently obtained under "soft chemistry" conditions through removal of the two

---

* To whom correspondence should be addressed.

lithium atoms from the ternary Li_2FeS_2 phase (1). This new, rather amorphous, FeS_2 has been characterized by Mössbauer, EXAFS, and infrared spectroscopies (2–4). These studies led to the charge balance Fe^{3+} $[(S_2)^{2-}]_{\frac{1}{2}} S^{2-}$, with Fe^{3+} cations in tetrahedral environments and with S^{2-} anions and $(S_2)^{2-}$ pairs. We are clearly dealing with an electronic structure intermediate between the 2D-dichalcogenides $M^{4+}(X^{2-})_2$ and the 3D pyrite type compounds $M^{2+}(X_2)^{2-}$. The electronic structure results from the competition between the anionic and the cationic oxidation states, involving the relative stability of the cationic (d) orbitals and anionic (p) band levels.

Relative to previous results on structurally related MX_2 compounds, it appears that the IrX_2 (X = S, Se) phases are good candidates; according to previous X-ray diffraction results (5) and recent more accurate X-ray powder data (6), the IrX_2 phases appear to display a similar charge balance Ir^{3+} $[(X_2)^{2-}]_{\frac{1}{2}}X^{2-}$, with the Ir^{3+} (d^6) cations distributed on two kinds of distorted octahedral environment. By contrast, Fe^{3+} filled tetrahedral sites. Moreover, abnormally long bond lengths in the chalcogen pairs were found in IrX_2 (d_{S-S} = 2.30 Å and d_{Se-Se} = 2.56 Å), along with an unexpected very small calculated effective cationic radius $[r(Ir^{3+})$ = 0.50 Å]. Such unusual structural features remain to be explained. A better understanding of the electronic properties of these IrX_2 phases, which contain various redox centers, is necessary to determine their suitability as high energy density cathode materials.

Therefore, an electronic and vibrational study of the IrS_2 and $IrSe_2$ phases and lattice dynamics calculations for IrS_2 were initiated in order to obtain better insight on their structural and electronic properties and to acquire relevant information before performing band-structure calculations. As far as we know, no vibrational study of these IrX_2 compounds has been reported. This

work has been undertaken as part of a more general electronic and vibrational study of chalcogen phases containing X^{2-} ions and $(X_2)^{2-}$ pair anions. In particular, we recently investigated the structural, optical, and electronic properties of MS_3 semiconductors with M = Ti^{4+}, Zr^{4+}, Hf^{4+} (7–9), or Mo^{5+} (10), along with the vibronic properties of the broad-band 2D semiconductor NbS_2Cl_2 (11), and those of the narrow band NbS_3 compound (12). In the last case we obtained new insight into the nature and the symmetry of the first excited electronic states from Raman studies under preresonance and exact resonance conditions. It was concluded that two overlapping electronic transitions in the visible region arise mainly from NbS states of nonbonding character and from the antibonding component (σu^*) of the closely bonded $(S_2)^{2-}$ pairs: these results constitute an interesting basis for a detailed analysis of the electron transfer in the related lithium intercalated Li_xNbS_3 compounds (12).

We have here recorded and analyzed the electronic spectra (from 300 to 900 nm) and the vibrational (infrared and Raman) spectra (from 500 to 10 cm^{-1}) of IrS_2 and $IrSe_2$ powder samples; in particular, we used various exciting laser lines (from 676.4 to 457.9 nm) in order to obtain the Raman intensity excitation profiles for many modes and new information about the main electronic transfers and localizations. In addition, following a recent lattice dynamics study of the pyrite and marcasite FeS_2 compounds (13), we have performed comparative valence force field calculations for the IrS_2 phase to check the main vibrational assignments and to better describe the nature and the form of all the crystalline normal modes. When several potential function parameters from related compounds are employed, one obtains more reliable results in terms of stretching and bending internal forces by use of valence force field type calculations (11–13).

Experimental

Powder samples with a controlled high purity of both IrS$_2$ and IrSe$_2$ phases were prepared as already described in Ref. (6). The UV–visible transmission spectra (from 300 to 900 nm) of samples dispersed in nujol at 300 K were recorded on a Philips PU 8700 instrument. Similarly, the mid-infrared (2000–200 cm^{-1}) and far-infrared (300–30 cm^{-1}) transmission spectra of nujol mulls were recorded on a Perkin–Elmer 983G spectrometer and on a Nicolet 20F interferometer, respectively. The resonance Raman spectra were obtained on a Dilor Z24 triple monochromator instrument using various emission lines of Spectra-Physics Kr$^+$ (676.4, 647.1, and 568.2 nm) and Ar$^+$ (514.5, 488.0, and 457.9 nm) lasers. Standard photon counting techniques were used for detection and frequency measurements were calibrated using plasma lines. The Raman excitation profiles were thus extracted from intensity mesurements in spectra of several homogeneous mixtures of the powders in RbClO$_4$ used as a standard; in all cases, the respective proportions were adjusted to minimize absorption effects of the incoming radiation and of the scattering light (12). Finally, the Raman spectra were obtained using a sample holder rotating at about 2000 rpm in order to minimize any local heating effects.

Structure and Selection Rules

According to recent accurate powder Rietveld calculations on IrS$_2$ and IrSe$_2$ (6), both IrX$_2$ phases belong to the *Pnam* (D_{2h}^{16}) space group. However, the *Pna2$_1$* (C_{2v}^9) noncentrosymmetric space group also fitted the intensity extinctions. The centrosymmetric group was found to yield the best results (6). One can expect to discriminate between both groups by examining the vibrational infrared and Raman activities. As a matter of fact, the primitive unit cells contain eight formula units of $[Ir^{3+}X^{2-}(X_2)_{\frac{1}{2}}^{2-}]$ type with all atoms located on *Cs* (*ab*) symmetry sites in the former case (Fig. 1), and on C_1 general positions in the latter one. The 72 (24 × 3) normal modes at the center of the Brillouin zone ($|k| = 0$) can thus be represented by the irreducible representations of the D_{2h} and C_{2v} point groups, respectively:

$$\Gamma(D_{2h}) = 12A_g + 12B_{1g} + 6B_{2g} + 6B_{3g}$$
$$+ (6A_u) + 6B_{1u} + 12B_{2u} + 12B_{3u}$$

and

$$\Gamma(C_{2v}) = 18A_1 + 18A_2 + 18B_1 + 18B_2.$$

Neglecting the acoustic modes, one thus expects 36 "gerade" Raman active modes plus 27 "ungerade" infrared active vibrations in the former case and 69 Raman active plus 51 infrared active modes in the latter case where many Raman–infrared coincidences for the $17A_1 + 17B_1 + 17B_2$ type vibrations must occur. Among these vibrations the stretching motions of $(X_2)^{2-}$ pairs should give rise to two Raman ($A_g + B_{1g}$) plus two infrared bands ($B_{2u} + B_{3u}$) in the D_{2h} point group and to four Raman ($A_1 + A_2 + B_1 + B_1$) plus three coincident infrared components ($A_1 + B_1 + B_2$) in the C_{2v} point group. Thus, it would be of great interest to determine the corresponding vibrations with confidence although some difficulties could arise due to the abnormally long chalcogen–chalcogen distances in $(X_2)^{2-}$ pairs, equal to 2.30 Å (S–S) and 2.56 Å (Se–Se). For regular pairs distances one would expect values close to 2.05 Å (14–16) and 2.35 Å (17, 18) in such semiconducting phases, i.e. smaller by about 10%. The origin of these long X–X distances in IrX$_2$ phases has been the subject of a preliminary discussion in Ref. (6).

Finally, as first pointed out by Barricelli (5), the respective octahedral and tetrahe-
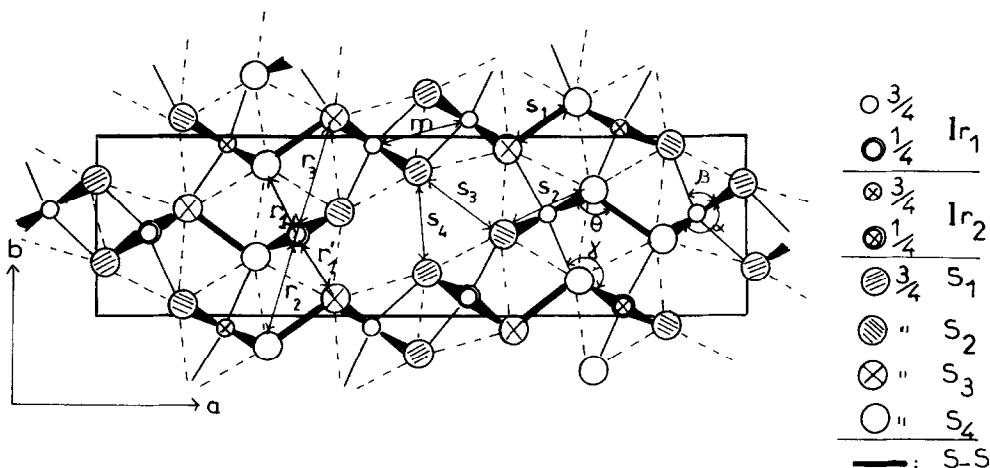
FIG. 1. Crystal structure of IrS_2 projected along the c axis and definition of the internal coordinates used in the valence force field calculations. Only atoms in the primitive unit cell with their first neighbor contacts are shown. Note the two kinds of Ir^{3+} ions (Ir_1, Ir_2) and the four kinds of sulfur ions (S_1 to S_4), half of them included in the (S_2) pairs; the dashed lines correspond to edges of the distorted octahedral Ir^{3+} environments.

dral environments of the iridium and chalcogen atoms allow one to compare the structures of IrX_2 and FeS_2 marcasite type compounds: in IrX_2 phases, only half of the chalcogen atoms are bonded to each other, there are three long and three short $Ir-X$ octahedral bond distances. By contrast, in the marcasite structure all chalcogen atoms are bonded in pairs; usually, two short and four long $Fe-X$ bond distances are found. However, ($S-S$) bond distances in FeS_2 marcasite are already quite large and significantly stretched (2.21 Å) as compared to values reported in CoS_2 (2.12 Å), FeS_2 pyrite (2.17 Å), and even RuS_2 (2.18 Å) compounds (19, 21). Moreover, the following differences are noteworthy: the axial ratios in IrS_2 ($a/b/c$ = 3.519/1.0/0.634) and $IrSe_2$ ($a/b/c$ = 3.529/1.0/0.630) represent an a/b value nearly four times greater than in the marcasite FeS_2 structure ($a/b/c$ = 0.838/1.0/0.626). Therefore, although a simple relationship between the vibrational properties of IrX_2 and FeS_2 compounds cannot be expected, one may assume in first approxima-

tion that a quadrupling of an $[IrX_2]_2$ "subunit cell" produces the folding of "sub-Brillouin zone" modes along the $a*$ reciprocal direction into the zone center. Thus, for some rather flat optic branches covering a narrow range in energy, the $|k| = 0$ phonons in IrX_2 could arise from $|k| = 0$, $|k| = a*/4$ and $|k| = a*/2$ phonons belonging to the same branch and produce frequency splittings and vibrational triplets. This approach will be discussed further in the analysis of the vibrational results.

Results and Discussion

In Section I, we shall successively present and analyze the electronic and vibrational spectra of both IrS_2 and $IrSe_2$ compounds. Results of complete normal coordinate calculations in the IrS_2 crystal will be discussed in Section II in order to establish many vibrational assignments. Finally, in Section III, the resonance Raman excitation profiles of various crystalline modes in IrS_2 and $IrSe_2$ will be analyzed in order to obtain new
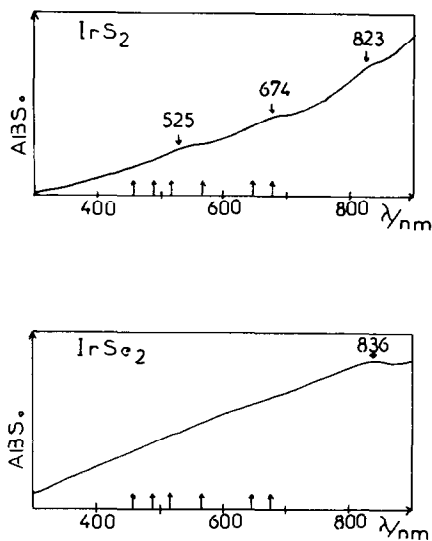
FIG. 2. The UV–visible electronic absorption spectra of IrS$_2$ and IrSe$_2$ at 300 K in the 300- to 900-nm range. Arrows indicate the main Kr$^+$ and Ar$^+$ laser Raman exciting lines.

information about the electronic properties of the phases.

I. Electronic and Vibrational Results

Electronic spectra. The UV–visible absorption spectra (300–900 nm) of powder samples of IrS$_2$ and IrSe$_2$ at 300 K are shown on Fig. 2. Surprisingly we observe a monotonic decrease in absorbance as the energy increases, with weak maxima at about 823, 674, and 525 nm in IrS$_2$ and at about 836 nm in IrSe$_2$, probably due to d–d type or ligand to metal charge transfer transitions. These features suggest the existence of more intense electronic bands in the near and mid infrared regions (see below), which confirms that we are dealing with very narrow-band semiconducting phases with strong metallic characteristics (5, 6). Indeed, the good agreement between some observed and calculated metallic distances, together with the fact that the compounds have a small and almost temperature-independent diamagne-

tism and a metallic luster, indicates that the (X_2) pairs and the three longer Ir–X bonds are metallic in character. This could be due to electrons of the X atoms being excited into the conduction band or possibly, to the nonstoichiometric composition of the phases (5, 6). In any case, when using laser excitations in the visible region, Raman experiments under postresonance conditions should provide new information about the nature of the electron transfers that constitute some of the $5d^6$ $6s^0$ (Ir^{3+}) and $3s^2$ $3p^6$ (S^{2-}) or $4s^2$ $4p^6$ (Se^{2-}) metallic like orbitals.

Infrared and Raman spectra. The infrared absorption and Raman scattering (λ_0 = 676.4 nm) spectra of IrS$_2$ and IrSe$_2$ polycrystalline samples, in the 450–10 cm^{-1} region, where all fundamental vibrations are expected, are shown in Figs. 3 and 4, respectively. The corresponding band wavenumbers, relative intensities, frequency ratios, and some tentative assignments are assembled in Table I.

The vibrational spectra show that all the fundamentals are localized in the 450–20 cm^{-1} range for IrS$_2$ and in the 310–20 cm^{-1} region for IrSe$_2$. Surprisingly, there are numerous quite sharp lines with many crystal field band splittings (Table I) as generally encountered in molecular crystals. Nevertheless, the infrared patterns in the higher energy regions also exhibit significant absorption increases which resemble low energy plasmon excitations. This corroborates the partial metallic character in the IrX_2 phases, but could also derive from holes in the anionic valence bands, leading to n-type semiconducting behavior and to the limit formula Ir^{3+} $X^{1.5-}$ [$(X_2)^{3-}$]$_\frac{1}{2}$, as previously proposed (6).

Careful inspection of the infrared and Raman band wavenumbers reveal few accidental coincidences; roughly 24 signals in IrS$_2$ and IrSe$_2$ are observed in both infrared and Raman spectra. These spectra are consistent only with those expected for the *Pnam* space group (D_{2h}^{16}), which definitely elimi-
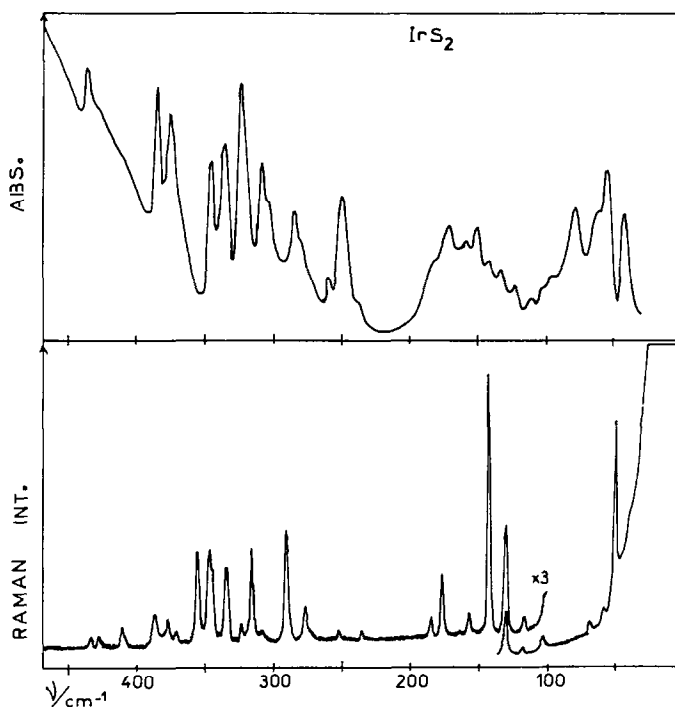
FIG 3. The infrared absorbance and Raman scattering (λ_0 = 676.4 nm) survey spectra (470–30 cm^{-1}) of IrS$_2$ at 300 K recorded using a mean resolution of 4 and 3 cm^{-1}, respectively.

nates [in agreement with (6)] the previously suggested Pna2$_1$ (C_{2v}^9) space group (5).

Concerning vibrational and symmetry assignments, only tentative arguments can be advanced, due to the unavailability of single crystal data. Nevertheless, based upon the observed relative band intensities and frequency ratios ν(IrS$_2$)/ν(IrSe$_2$), one can distinguish five groups of bands (Table I). First, we propose to assign the intense infrared bands and weak Raman components in the 450–360 cm^{-1} region for IrS$_2$ and in the 303–260 cm^{-1} range for IrSe$_2$ to asymmetric stretching ν_{asym} IrX_3 type modes; these bands give rise to frequency ratios ranging from 1.45 to 1.52. The second group is composed of intense infrared and Raman signals in the 360–270 cm^{-1} (IrS$_2$) and 230–170 cm^{-1} (IrSe$_2$) ranges, yielding ratios equal to 1.52–1.56. These bands may be assigned to

symmetric stretching ν_{sym} IrX_3 vibrations, with some of them probably coupled to the $\nu(X-X)$ stretching modes expected in this region. Indeed, under the assumption of isolated (S–S)$^{2-}$ pair anions, one predicts from the Steudel's relation (22) (which works nicely in many related sulfur compounds (16)) that d(S–S)$^{2-}$/Å = 2.57–9.47 × 10^{-4} ν(S–S)/cm^{-1}, and a band wavenumber of 285 cm^{-1}. We have for the first time identified this mode at 323 cm^{-1} in the Raman spectrum of FeS$_2$ marcasite (13). Thus, in contrast to many $M^{IV}X_3$ compounds with X = S, Se (7–9, 23, 24) we confirm that the IrX_2 phases do not exhibit characteristic high frequency signals associated with strongly bonded (X_2) pairs, giving rise to a large frequency ratio (~1.7) on going from sulfide to selenide phases (23). This is in agreement with the high oxidation state of
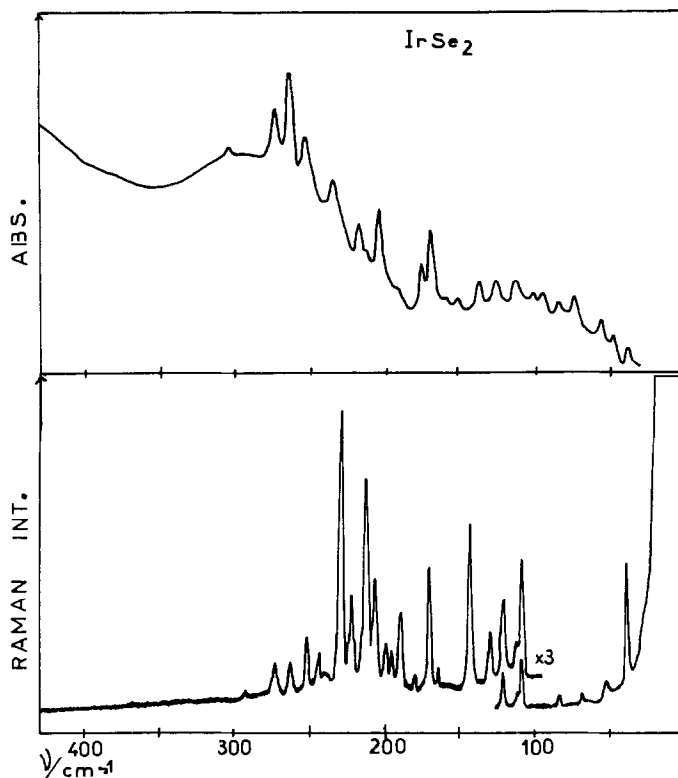
FIG. 4. The infrared absorbance and Raman scattering (λ_0 = 676.4 nm) survey spectra (430–30 cm^{-1}) of IrSe$_2$ at 300 K recorded using a mean resolution of 4 and 3 cm^{-1}, respectively.

the $(X_2)^{3-}$ pairs as inferred in Ref. (6). A confident assignment of these vibrations can only be made through normal coordinate calculations (see below). Subsequently, the intense infrared absorptions and weak Raman counterparts in the 260- to 200-cm^{-1} and 170- to 155-cm^{-1} ranges form a third group, with a ratio equal to 1.49, while numerous bands in the 200–100 cm^{-1} and 155–80 cm^{-1} regions are collected in a fourth group showing ratios of 1.22–1.24 (Table I). In first approximation, we suggest that frequency scaling between vibrations of orthorhombic IrS$_2$ and IrSe$_2$ derives from scaling between the bond stretching and the angle-bending wavenumbers of the "IrX_3" local groups. These subunits derive from the three short and three large Ir–X distances in

the IrX_6 environments from which the 3D network of the crystal is constructed. We thus propose to assign the bands of the above-mentioned groups to ν_{asym}, ν_{syn}, δ_{asym}, and δ_{sym} (IrX_3) type vibrations, respectively, although bands in the last group are probably coupled with complex crystalline deformation modes. As a cross-check we have used the simplified formula for IrX_3 pyramidal groups (25) and, under the crude assumptions of identical bonding and bending force constants in IrS$_2$ and IrSe$_2$, we have calculated the corresponding scaling ratios to be equal to 1.42, 1.46, 1.45, and 1.33, respectively. These values match experiment reasonably well, considering that the model is not expected to be very accurate since it neglects coupling between the

TABLE I

BAND WAVENUMBERS (cm⁻¹), RELATIVE INTENSITIES, FREQUENCY RATIOS AND TENTATIVE ASSIGNMENTS OF THE INFRARED AND RAMAN
(λ_0 = 676.4 nm) SPECTRA OF IrS₂ AND IrSe₂ AT 300 K

| IrS₂ | | | | | IrSe₂ | | | | | $\nu(IrS_2)/\nu(IrSe_2)$ | | Tentative assignments |
| IR[a] | | Raman | | | IR[a] | | Raman | | | | | |
ν(cm⁻¹)	Intensity	ν	Intensity	$f(\lambda_0)$[b]	ν/cm⁻¹	Intensity	ν/cm⁻¹	Intensity	$f(\lambda_0)$[b]	IR	Raman	
438	m	434	w	~6	303	vw	291	w		1.45	1.49	
430	vw	428	w		—							
—		410	m		272	m	272	m	~8		1.51	
385	s	386	m	22	262	m	261	m		1.47	1.48	$\nu_{asym}(IrX_3)$
376	s	376	m		253	m	251	m	~4	1.49	1.50	
		370	w		250	sh	243	m			1.52	
		355	s	8			229	s	22		1.55	
346	s	346	s	9	233	m	222	m	~9	1.48	1.56	
		344	sh									
336	s	334	s	11	216	m	213	s	~13	1.56	1.57	
324	s	324	w		210	w	207	m	~8	1.54	1.57	$\nu_{sym}(IrX_3)$
		316	s	20			199	w			1.59	+ $\nu(X-X)$?
308	s	308	vw		203	s	195	w		1.52	1.58	
285	m	291	s	13	190	w	189	s	7	1.50	1.54	
							180	vw				

ν	I	~7	ν	I	~7	ν	I	~7	ν	I	~7	$f(\lambda_0)$	$f(\lambda_0)$	Assignment
277	sh	~7	276	m	~7	—	m	~7	170	s		1.49	1.62	$\delta_{asym}(IrX_3)$
259	w		253	vw		174	m		163	vw		1.49	1.55	
250	s		235	w		168	m		—			1.48		
234	vw		184	m		158	w		—			1.21		
182	sh		176	m	~10	151	m		142	s	14	1.27	1.24	
172	m	~10	157	m		135	m	~10	128	m		1.24	1.23	$\delta_{sym}(IrX_3)$ + deformation modes
153	m		143	vs	11	123	m		120	s	15		1.19	
144	w	11	130	s		—		11	110	sh		1.21	1.20	
133	m	10	116	w	10	110	m	10	108	s	5	1.24		
122	m		102	w		98	m		82	w		1.20	1.24	
112	vw		67	vw		93	m		67	w		1.28		T' lattice modes
104	vw		56	vw		81	w		51	vw		1.23		
86	w		48	s		70	w		38	s		1.30	1.31	
70	m					54	vw		—			1.20		
54	m					45							1.26	
—						—						1.20		
42	m					34	w					1.23		

[a] Relative intensities are indicated with vw = very weak, w = weak, m = medium, s = strong, vs = very strong, and sh = shoulder.

[b] $f(\lambda_0)$ values are the Raman enhancement factors for $\lambda_0 = 676.4$ nm relative to data at 457.9 nm (experimental errors $\pm 5\%$).

various pyramidal groups that compose the framework of the crystal structure. Nevertheless, as in layer type compounds such as arsenic chalcogenides, As_2X_3 (26, 27), this simple model roughly shows how the frequency scalings arise from structural similarities.

Finally, in the very low frequency parts of the spectra ($\nu \leqq 90$–70 cm^{-1}), the observed bands display frequency ratios ranging from 1.20 to 1.31 and thus are tentatively assigned to translational lattice modes; in effect, for concerted T' motions of IrX_3 or IrX_6 groups the square roots of reduced mass ratios are expected to be equal to 1.22 or 1.32.

One should note that several vibrational bands appear as triplets (see for instance at about 376, 346, 316, and 250 cm^{-1} in IrS$_2$) with small frequency splitting roughly equal to 10–20 cm^{-1}. As already discussed, this could be due to a quadrupling, along the a^* reciprocal direction, of the [IrX_2]$_2$ "subunit cell," similar to that in the orthorhombic marcasite FeS$_2$ compound. Nevertheless, as expected from large internal structural differences, the vibrational properties of both IrS$_2$ and FeS$_2$ (13, 27) compounds are not closely related.

II. Valence Force Field Calculations and Lattice Dynamics

Using the above vibrational data, we carried out valence force field calculations to determine precisely the nature of all the normal modes, to address the problem of the anomalously long stretched chalcogen pairs, and to check for the existence of constraints in these structural phases.

It was also of interest to obtain new information about the various phonons which exhibit large intensity enhancements under resonance Raman conditions (see below). Using a valence force field quite similar to that recently applied to pyrite and marcasite FeS$_2$ compounds (13), we calculated the wavenumbers of all fundamentals, their main potential energy distributions, and the
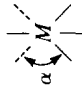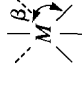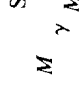
mean square vibrational amplitudes. The final values of force constants are listed in Table II and the main results are reported in Table III and illustrated in Fig. 5.

Internal coordinates and potential function. From the atomic cartesian coordinates in the crystal structure (6), we identify nine principal stretching coordinates, two that relate to the Ir–S (r_1 and r_1') short and long Ir–S distances, one for the S–S (s_1 for the pairs)-bonded atoms, and the remaining six that involve the Ir···S (r_2, r_3), Ir···Ir (m), and S···S (s_2, s_3, s_4) shortest contacts between nonbonded atoms.

These definitions take into account the possible metal to sulfur interactions at 3.535 Å (r_2) and at 3.628–3.657 Å (r_3) along the **b** direction, whereas metal to metal contacts (m) in the (ac) planes are considered to operate between IrS$_6$ octahedra sharing edges; the latter definitions include the shortest intraoctahedra S···S distances (3.003 and 3.079 Å for s_2) and the S···S interoctahedra interactions inside the empty channels of the crystal structure. The s_3 and s_4 coordinates correspond to interatomic distances of 3.203 and 3.570 Å, respectively (Fig. 1). The s_2 and s_3 force constants correspond to contacts in between IrS$_6$ octahedra sharing a corner. In such a potential function, all atom–atom interactions up to 3.66 Å for Ir···S, 3.63 Å for Ir···Ir and 3.57 Å for S···S atoms are taken into account; as previously demonstrated in establishing the valence force fields of FeS$_2$ pyrite and marcasite type compounds (13), these long range interactions may play an important role in such constrained 3D crystal structures.

Similarly, we define twelve bending coordinates around each IrS$_6$ environment (α and β types) and six bending ones around each tetrahedral sulfur surrounding (γ and θ types). These environments are strongly distorted so that α, β angular values are distributed over the 81–108° range and γ, θ values vary from 79° up to 131°. Nevertheless, for simplicity, we have constrained

TABLE II

VALUES OF PRINCIPAL AND INTERACTION FORCE CONSTANTS[a] IN IrS$_2$ AND COMPARISON WITH CORRESPONDING CONSTANTS IN PYRITE AND MARCASITE FeS$_2$ COMPOUNDS (13); BOND DISTANCES (Å) AND SOME BOND ANGLES (°) ARE INDICATED IN PARENTHESES

Stretching definitions

Compounds	$r_1(M-S)$	$r_2(M\cdots S)$	$r_3(M\cdots S)$	$m(M\cdots M)$	$s_1(S-S)$	$s_2(S\cdots S)$	$s_3(S\cdots S)$	$s_4(S\cdots S)$
FeS$_2$ pyrite	(2.262) 1.20	(3.454)−0.07	(3.603) 0.20	(3.831) 0.20	(2.177) 0.90	(3.074) 0.16	(3.320) 0.10	—
FeS$_2$ marca.	(2.23–2.25) 1.03	(3.482)−0.07	(3.597) 0.10	(3.886) 0.30	(2.212) 0.70	(3.114) 0.35	(3.222)−0.03	—
IrS$_2$ r_i(2.315)	1.30	(3.535)	(3.628–3.657)	(3.630)	(2.30)	(3.00–3.08)	(3.203)	(3.570)
IrS$_2$ r_i'(2.385)	1.10	0.10	0.10	0.20	0.60	0.10	0.15	0.10

Bending

Compounds	α $\overset{}{M}$	β M	$S\ \gamma\ M$ M	S θ S M M
FeS$_2$ pyrite	(~90°) 0.50	(~90°) 0.30	(115.7°) 0.20	(102.1°) 0.20
FeS$_2$ marca.	(83–97°) 0.40	(88–92°) 0.55	(97–120°) 0.20	(103–107°) 0.20
IrS$_2$	(81–101°) 0.40	(84–95°) 0.30	(97–101°) γ′ = 0.30 (117–123°) γ = 0.20	(79–131°) 0.20

Stretch–stretch interactions

Compounds	f_{r_1}/r_1 or r_1'/r_1'	f_{r_1}/r_1 "trans"	f_{r_1}/s_1	$f_{r_1}M\text{-}S/r_f S\text{-}M'$
FeS$_2$ pyrite	0.20	0.0	0.4	0.4
FeS$_2$ marca.	0.13	0.2	0.4	0.4
IrS$_2$	0.20	—	—	—

[a] Stretching and bending constants are given in 10^{2}N/m and Nm/rad^2, respectively.

TABLE III

COMPARISON OF OBSERVED AND CALCULATED BAND WAVENUMBERS (cm^{-1}) AND VALUES OF THE MAIN POTENTIAL ENERGY DISTRIBUTIONS (P.E.D. $\geq$ 4.0%) IN A_g AND B_{2u} TYPE MODES

ν(cm^{-1})		Symmetry	P.E.D.%								
Raman observed	Raman calculated		(Ir–S)		(Ir···S)	Ir···Ir	(S–S)	S···S	[Ir] ($\alpha + \beta$)	[S] ($\gamma + \theta$)	
			r_1	r'_1	$r_2 + r_3$	m	s_1	$s_2 + s_3 + s_4$	$(\alpha + \beta)$	$(\gamma + \theta)$	
434 w	457.7	B_{1g}									
428 w	427.7	A_g	29.9	28.1				4.6	8.7	6.8	
410 m	400.1	B_{1g}									
386 m	385.1	A_g	71.5	10.1					9.7	9.5	
376 m	370.8	B_{1g}									
370 w	368.4	A_g	49.1	22.7			8.8	5.4	13.6	11.1	
	362.7	$B_{2g}\ B_{3g}$									
355 s	355.6	B_{3g}	54.4	23.8					10.1	11.3	
346 s	345.8	$A_g\ B_{1g}$	3.8	43.8				18.5	15.6	10.9	
344 sh	340.9	B_{2g}									
334 s	330.5	B_{1g}	10.1	12.5			46.0		19.5	11.5	
324 w											
316 s	320.1	A_g	20.3	8.2	4.3		46.8		9.6	12.6	
308 vw	286.8	B_{1g}									
291 s	284.5	A_g	36.1	84.0				8.1	11.2	10.7	
276 w	275.0	$B_{2g}\ B_{3g}$		58.2					9.5	24.7	
	268.2	B_{3g}									
	256.9	B_{3g}									
253 vw	252.5	B_{2g}									
235 w	236.0	$A_g\ B_{1g}$	27.2	21.3					24.8	17.2	
	234.6	B_{1g}									
184 m	228.2	B_{1g}									
176 m	225.8	A_g	28.6	14.6	4.0			5.9	33.9	18.8	

Infrared observed	Infrared calculated	Symmetry	r_1	r_1'	$r_2 + r_3$	m	s_1	$s_2 + s_3 + s_4$	$(\alpha + \beta)$	$(\gamma + \theta)$
438 m	460.3	B_{3u}	25.7	28.5					9.1	6.8
430 vw	434.3	B_{2u}						5.3		
—	404.4	B_{3u}								
385 s	386.0	B_{2u}	69.6	11.3					9.9	9.0
376 s	371.2	B_{3u}	45.4	25.3			7.8	5.9	13.7	9.2
	370.0	B_{2u}								
—	363.5	B_{1u}								
	(362.1)	A_u								
—	359.9	B_{2u}	17.5	51.7					13.2	10.7
	358.6	B_{3u}								
—	355.2	B_{1u}			4.1					
346 s	(348.4)	A_u								
336 s	331.5	B_{3u}	10.5	10.2			47.7		21.1	11.1
324 s	321.7	B_{2u}	19.5	8.2			46.5		10.3	12.3
308 s	271.8	B_{3u}								
285 m	271.3	B_{2u}		66.7					20.7	18.1
277 sh	270.6	B_{1u}								
	(261.4)	A_u								
	(255.5)	A_u								
		B_{1u}								
259 w	246.9	B_{3u}								
250 s	236.0	B_{2u}								
234 vw	235.0	B_{1u}	22.2	25.4				9.8	18.9	19.6
182 sh	230.7	B_{2u}	28.5	11.7	4.9			7.4	33.3	17.8
157 m	146.6	B_{1g}	12.4	5.8		13.0		4.3	36.1	25.6
143 vs	146.4	A_g	18.5	15.3		13.3	3.7		23.8	20.5
130 s	130.6	B_{1g}	11.7	16.5		6.2			36.2	26.2
116 w	112.7	A_g	20.3	25.4				9.4	31.0	16.4
	108.4	A_g	16.6	6.9			4.0		34.6	28.3
102 w	101.3	B_{2g} B_{3g}			5.6					
—	80.6	B_{2g}								
—	76.2	B_{1g}								
67 vw	68.0	B_{1g}								
56 vw	44.5	A_g	23.3	15.6				17.9	29.7	16.1
48 s	42.7	B_{3g}								

TABLE III—Continued

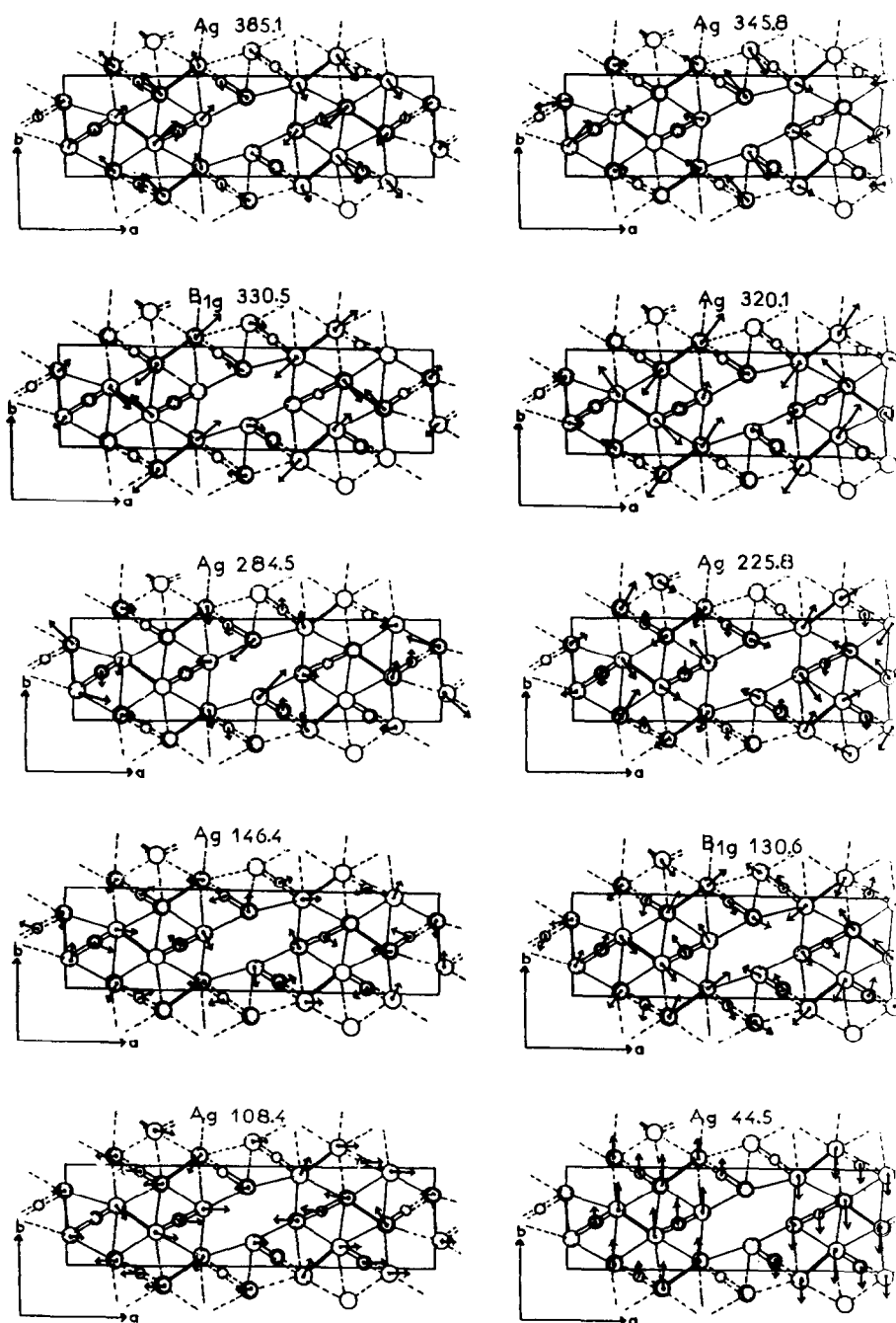| Infrared observed | Infrared calculated | Symmetry | P.E.D.% | | | | | | | |
			(Ir–S)		(Ir···S)	Ir···Ir	(S–S)	S···S		
			r_1	r_1'	$r_2 + r_3$	m	s_1	$s_2 + s_3 + s_4$	$(\alpha + \beta)$	$(\gamma + \theta)$
172 m	227.7	B_{3u}								
153 m										
144 w										
133 m	129.4	B_{3u}								
122 m										
112 vw	111.9	B_{2u}	18.6	6.5	6.5			7.3	33.0	28.0
104 vw	109.1	B_{3u}								
	(92.7)	A_u								
86 w	91.9	B_{2u}	22.3	31.0				4.3	35.0	18.6
—	76.6	B_{1u}								
70 m	74.2	B_{2u}	21.5	6.2			23.2	5.9	14.9	17.8
54 m										
42 m	48.7	B_{3u}								
	(43.9)	A_u								
—	0.0	B_{1u} B_{2u} B_{3u}								

FIG. 5. Scheme for the calculated relative main atomic displacements in IrS₂ associated with some selected high-frequency and low-frequency Raman vibrational modes.

many bending constants to have identical values and we have considered only five distinct parameters (Table II). For the same reason we have constrained to zero most stretch–stretch off-diagonal force constants and ignored all the stretch–bend interactions; however, the stretch–stretch constants (f_{r_1/r_1} or $f_{r_1'/r_1'}$) for Ir–S bonds in "*cis*" positions were included because the quality of the fits was thereby significantly improved.

Secular determinants for the eight symmetry blocks of the D_{2h} orthorhombic structure were determined according to the F_{XSM} method, the mass-weighted cartesian symmetry force constant matrix, as first described by Shimanouchi (28). Force constants were adjusted by minimizing the fractional deviations of calculated band wavenumbers from the observed values by a least-squares process. However, due to the lack of vibrational polarization data, only the results for the four Raman blocks ($A_g + B_{1g} + B_{2g} + B_{3g}$) and the three infrared active blocks ($B_{1u} + B_{2u} + B_{3u}$) were compared to experimental data. Therefore, many force constants were transfered from the valence force fields of the FeS_2 compounds without appropriate refinements and must be considered as tentative. It is remarkable that we used only fifteen distinct parameters in the potential function to calculate a total of 36 Raman and 36 infrared (only 30 infrared active) phonon wavenumbers.

Force constants, calculated wavenumbers, and description of the normal modes. As shown in Table II, values of the proposed force constants are comparable to those in pyrite and marcasite FeS_2 compounds.

Although the Ir^{3+} ions belong to two distinct crystalline families and possess markedly distorted environments, only two principal Ir–S stretching force constants are adjusted to 1.3×10^2 Nm^{-1} and 1.1×10^2 Nm^{-1} for the corresponding short and long bondings. These values play an important

role in fitting the band wavenumbers in the 450–250 cm^{-1} region; they correspond to significant bonding no matter what kind of sulfur anion S or (S–S) considered. We have determined recently quite similar metal to sulfur force constants in NbS_2Cl_2 [1.10×10^2 N m^{-1}, Ref. (11)] and NbS_3 [1.3 and 1.1 $\times 10^2$ N m^{-1} (12)] compounds; these values compare well with those proposed in the literature for $3R$–NbS_2 (1.34×10^2 N m^{-1}) and $2H$–NbS_2 (1.14×10^2 N m^{-1}) (29). By contrast, the stretching (S–S) force constant is confirmed to be anomalously small, 0.6 $\times 10^2$ N m^{-1}, even smaller than in FeS_2 marcasite (0.7×10^2 N m^{-1}), as would be expected from interatomic distance inspections. When compared with the large values, equal to 2.36×10^2 N m^{-1} and 2.48×10^2 N m^{-1}, found in NbS_2Cl_2 and NbS_3 compounds (11, 12) which possess firmly bonded $(S_2)^{2-}$ pairs (2.00 and 2.05 Å), it is tempting to conclude that these units in the IrS_2 phase have accommodated electrons within the antibonding σ_u^* (3p)) orbitals and should be described as $(S_2)^{3-}$ anions. The charge balance in IrS_2 would thus be represented by the limit formula ($Ir^{3+} S^{1.5-}[(S_2)^{3-}]_{\frac{1}{2}}$) in which all the sulfur atoms are in the -1.5 oxidation state. Interestingly, the $Ir\cdots S$, $Ir\cdots Ir$, and $S\cdots S$ stretching force constants between nonbonded atoms again show nonnegligible values as in the FeS_2 compounds; an additional constant (s_4) between sulfur ions at a distance of 3.57 Å in the IrS_2 phase cannot be neglected: this confirms the occurrence of many constraints between the various edge sharing or corner sharing IrS_6 octahedra of the crystal structure. The above results are in disagreement with Barricelli's conclusions (5) that the structure of IrX_2 phases involves layers with metallic bond character alternating with layers of normal covalent bonds perpendicular to the a axis, since the Ir–S stretching forces are comparable from one layer to another and many interlayer interactions are effective.

Reasonable values are also proposed (Ta-

ble II) for the bending constants and stretch–stretch interactions, but these values are not accurately determined as previously discussed.

Finally, the proposed valence force field shows that our assumption of separating crystalline vibrations into internal and external modes of IrX$_3$ units is a very crude approximation; thus, we are dealing with a truly ionocovalent 3D structure in which complex normal modes are encountered.

As shown in Table III, the overall agreement between observed and calculated band wavenumbers seems to be quite good for the Raman modes and satisfactory for the infrared bands, considering the approximations used. Some discrepencies appear between observed and calculated infrared components in the 310–280 cm^{-1} and 200–150 cm^{-1} regions. Better agreements could be obtained, but more refined calculations must await polarization data on single crystals. From inspection of the main potential energy distributions (Table III), we confirm that the high-frequency bands in the 440–340 cm^{-1} region are due to stretching motions in IrS$_6$ units; the Raman bands observed at 334 cm^{-1} (B_{1g}) and 316 cm^{-1} (A_g) and their infrared counterparts at 336 cm^{-1} (B_{3u}) and 324 cm^{-1} (B_{2u}) contain large contributions due to stretching modes of (S_2) pairs. However, these modes are partly coupled with Ir–S elongations whose contributions are still dominant for some modes down to 290 cm^{-1}. The lower frequency signals in the 280–100 cm^{-1} region are complex mixtures of stretching and bending motions of Ir–S$_6$ entities, the bending contributions becoming predominant in the lowest frequency modes. Finally, long-range interactions between nonbonded Ir^{3+} and sulfur atoms do not play an important role, whereas interactions between sulfur atoms seem effective for many modes and nonnegligible metal–metal interactions (~6–13% in P.E.D.) are predicted for some Raman bands located in the 160–130 cm^{-1} range.

All this information will later be discussed in connection with the Raman excitation profiles observed under resonance conditions; nevertheless, it is clear that, whatever the frequency range, the potential energy distributions due to the bending force constants cannot be neglected in the various normal modes: this again confirms the existence of large constraints inside and between the various IrS$_6$ units.

It is often meaningful to illustrate the normal crystalline modes by their mean square vibrational amplitudes. The atomic displacements calculated in some selected (mostly of A_g type) modes are shown in Fig. 5. In the upper part of the figure there are two A_g modes calculated at 385.1 and 345.8 cm^{-1} which involve only asymmetric stretching motions of the short and long Ir–S bonds, respectively. The two following modes calculated at 330.5 cm^{-1} (B_{1g}) and 320.1 cm^{-1} (A_g) clearly correspond to the Raman active stretching vibrations of (S_2) pairs, out-of-phase and in phase motions, respectively. These results definitely confirm the localization of the vibrations due to the anomalously stretched pair anions. The two complex A_g modes at 284.5 and 225.8 cm^{-1} are due to couplings between stretching and bending motions in the IrS$_6$ entities, a situation also encountered with the normal modes at 146.4 cm^{-1} (A_g) and 130.6 cm^{-1} (B_{1g}). However, in the latter cases the metal ions exhibit nonnegligible amplitudes so that metal–metal interactions are involved in their description. Finally, we have selected the two low frequency A_g type vibrations at 108.4 and 44.5 cm^{-1} which can be nicely compared to longitudinal and transversal acoustic modes along the (100) direction, respectively. These modes originate from the quadrupling along the a^* direction of the crystallographic unit cell.

In conclusion, the proposed valence force field model, although approximate, satisfactorily reproduces the experimental data and allows us to describe the nature and the form

of all the crystalline vibrations: As expected, we found some analogies in the lattice vibrational properties of both IrS_2 and FeS_2 marcasite compounds; in particular, low frequency stretching motions were found for the weakly bonded (S_2) pair anions and many interactions as well as large constraints between the various MS_6 distorted environments.

III. Resonance Raman Effects and Excitation Profiles

In the resonance Raman measurements, we used several homogeneous mixtures of the powders in $RbClO_4$ with concentrations ranging from 0.39 to 1.56 mmol/g for IrS_2 and from 0.64 to 1.14 mmole/g for $IrSe_2$. This allowed us to minimize absorption effects of both the incoming radiation and the scattered light, since the corresponding concentration maxima in pure products are equal to 3.90 and 2.86 mmole/g. Therefore, following the method already described (11), we obtained reliable Raman intensities for many modes using several excitation lines, leading to the excitation profiles displayed in Fig. 6.

Most of the modes under inspection correspond to the more intense A_g type Raman modes plus the B_{1g} type signals at 434, 334, and 130 cm^{-1}, the B_{2g} one at 276 cm^{-1}, and the B_{3g} mode at 355 cm^{-1} in IrS_2. As clearly evidenced in Fig. 6, on going from $\lambda_0 = 457.9$ nm to $\lambda_0 = 676.4$ nm excitations we encounter large Raman intensity enhancements probably due to postresonance effects, with electronic transitions in the visible and near-infrared regions. The magnitudes of these enhancements are largely mode-dependent in both IrS_2 and $IrSe_2$ compounds; indeed, although $IrSe_2$ appears as a better scattering sample, similar Raman intensity factors are generally observed for the corresponding modes in both compounds [$f(\lambda_0)$ in Table I]: these scaling factors vary in the 6–22 (IrS_2) and 4–22 ($IrSe_2$) ranges; the largest enhancements are detected on the totally symmetric vibrations

at 386, 316, 291, and 143 cm^{-1} in IrS_2. As discussed above, these modes contain large potential energy distributions of the force constants due to $r_1(Ir–S)$, $s_1(S–S)$, $r_1'(Ir–S)$, and $m(Ir\cdots Ir)$ stretching coordinates, respectively, with additional contributions on the bending coordinates: this implies significant modulation of the corresponding bond lengths and, to a lesser extent, of the bond angles in the electronic band responsible for these resonance effects. Indeed, according to the general rule stated first by Nishimura et al. (30), based on the behavior of Franck–Condon factors for totally symmetrical modes, the more enhanced modes at resonance are responsible for transforming the equilibrium geometry from that of the ground state to that appropriate to the resonant excited states. We thus conclude that the electronic transitions which involve a modulation of the (Ir–S) bonds, as well as of the (S–S) and (Ir–Ir) interatomic distances, are probably either of metal (Ir^{3+}) to ligand ($S^{1.5-}$) and/or ligand $(S_2)^{3-}$ to metal (Ir^{3+}) types or of intraligand nature $p(S_2)^{3-} \rightarrow p(S^{1.5-})$. Such electronic orbital excitations would finally stabilize the IrS_2 compound as represented by its more classic formula $Ir^{3+} S^{2-}[(S_2)^{2-}]_{\frac{1}{2}}$ in these excited states, from which d type electrons would be more easily excited. In fact, we are dealing with a very complex electronic system in which several charge-transfer states of B_{1u}, B_{2u}, or B_{3u} symmetry may not only interfere in the resonance Raman mechanism but may also be vibronically coupled. As a matter of fact the intensity enhancements of B_{1g}, B_{2g}, and B_{3g} symmetry modes can only be explained by vibronic couplings, and the d–d type electronically forbidden transitions may thus become partially vibronically allowed (31).

So, a more precise description of the structural changes and electron transfers in these resonant excited states must await complete electronic and structure calculations and additional experimental data. In this last respect, it is noteworthy that the
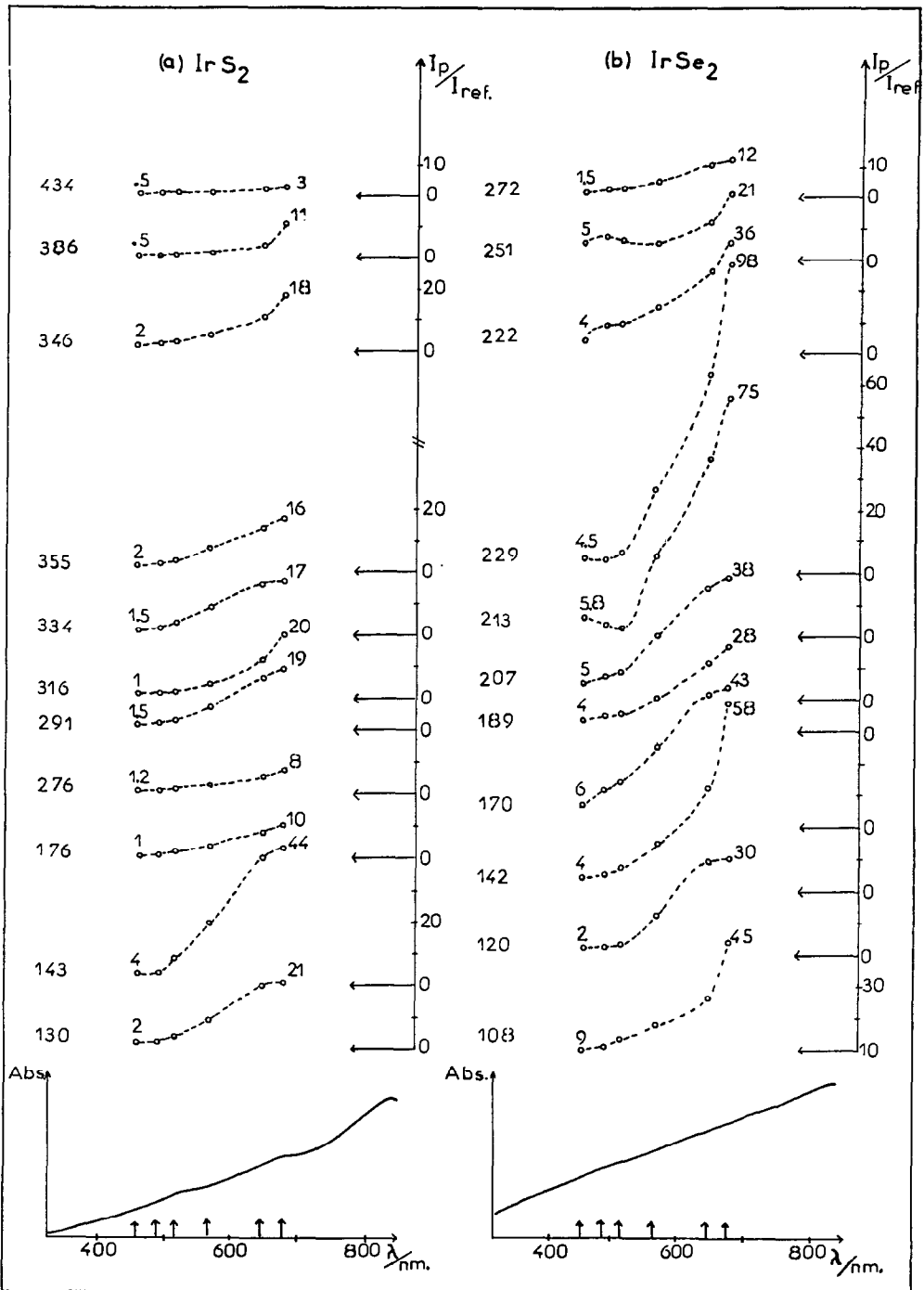
FIG. 6. Comparison of the electronic absorption spectra and of the relative Raman intensities in the 457.9- to 676.4-nm range for various modes in IrS₂ (a) and in IrSe₂(b) compounds. The dashed lines are guides and extreme relative intensities are indicated.

IrX_2 phases could be good candidates for new Fourier-transform resonance Raman experiments using the 1064-nm radiation of a Nd–YAG laser (32).

References

1. R. BREC, G. OUVRARD, AND E. PROUZET, *J. Power Sources* **26**, 3, 325 (1989).
2. L. BLANDEAU, G. OUVRARD, Y. CALAGE, R. BREC, AND J. ROUXEL, *J. Phys. C. Solid State Phys.* **20**, 4271 (1987).
3. P. GARD, C. SOURISSEAU, G. OUVRARD, AND R. BREC, *Solid State Ionics* **20**, 231 (1986).
4. R. T. BATCHELOR, F. W. B. EINSTEIN, C. H. W. JONES, R. FONG, AND J. R. DAHN, *Phys. Rev. B* **37**, 3699 (1988).
5. L. B. BARRICELLI, *Acta Crysallogr.* **11**, 75 (1989).
6. S. JOBIC, P. DENIARD, R. BREC, J. ROUXEL, M. DREW, AND W. E. DAVID, *J. Solid State Chem.* (1990), in press.
7. C. SOURISSEAU AND Y. MATHEY, *Chem. Phys.* **63**, 143 (1981).
8. S. P. GWET, Y. MATHEY, AND C. SOURISSEAU, *Phys. Status Solidi B* **125**, 503 (1984).
9. P. GARD, C. SOURISSEAU, AND O. GOROCHOV, *Phys. Status Solidi B* **144**, 885 (1988).
10. C. SOURISSEAU, O. GOROCHOV, AND D. M. SCHLEICK, *Mater. Sci. Eng. B* **9**, 113 (1989).
11. C. SOURISSEAU, P. GARD, AND M. FOUASSIER, *Chem. Phys.* **123**, 405 (1988).
12. C. SOURISSEAU, R. CAVAGNAT, M. FOUASSIER, AND P. MARAVAL, *J. Raman Spectrosc.* **21**, 337 (1990).
13. C. SOURISSEAU, R. CAVAGNAT, AND M. FOUASSIER, *J. Phys. Chem. Solids*, in press.
14. R. BREC, G. OUVRARD, M. EVAIN, P. GRENOUILLEAU, AND J. ROUXEL, *J. Solid State Chem.* **47**, 174 (1983).
15. M. EVAIN, M. QUEIGNEC, R. BREC, AND J. ROUXEL, *J. Solid State Chem.* **56**, 148 (1985).
16. M. QUEIGNEC, M. EVAIN, R. BREC, AND C. SOURISSEAU, *J. Solid State Chem.* **63**, 89 (1986).
17. M. EVAIN, M. QUEIGNEC, R. BREC, AND C. SOURISSEAU, *J. Solid State Chem.* **75**, 413 (1988).
18. A. MEERSCHAUT, P. PALVADEAU, AND J. ROUXEL, *J. Solid State Chem.* **20**, 21 (1978).
19. G. BROSTIGEN, A. KJEKSHUS, AND CHR. ROMMING, *Acta Chem. Scand.* **27**, 2791 (1973).
20. N. ELLIOT, *J. Chem. Phys.* **33**, 903 (1960).
21. G. BROSTIGEN, AND A. KJEKSHUS, *Acta Chem. Scand.* **24**, 2993 (1970).
22. R. STEUDEL, *Angew. Chem. Int. Ed. Engl.* **14**, 655 (1975).
23. A. ZWICK, M. A. RENUCCI, AND A. KJEKSHUS, *J. Phys. C. Solid State Phys.* **13**, 5603 (1980).
24. S. FURUSETH, L. BREITTAS, AND A. KJEKSHUS, *Acta Chem. Scand.* **A29**, 623 (1975).
25. K. NAKAMOTO, *in* "Infrared and Raman Spectra of Inorganic and Coordination Compounds," Wiley, New York (1986), p. 468.
26. R. ZALLEN AND M. L. SLADE, *Phys. Rev.* **B9**, 1627 (1974).
27. E. J. FLYNN, S. A. SOLIN, AND G. N. PAPATHEODOROU, *Phys. Rev.* **B13**, 1752 (1976).
28. T. SHIMANOUCHI, "Computer Programs for Normal Coordinate Treatments of Polyatomic Crystals," Tokyo (1968).
29. W. G. McMULLAN AND J. C. IRWIN, *Solid State Commun.* **15**, 557 (1983).
30. Y. NISHIMINA, A. Y. HIRAKAWA, AND M. TSUBOI, in "Advances in Infrared and Raman Spectroscopy," (R. J. H. Clark and R. E. Hester, Eds.), Vol. 5, p. 217, Heyden, London (1978).
31. P. STEIN, V. MISKOWSKI, W. H. WOODRUFF, J. P. GRIFFIN, K. G. WERNER, B. P. GABER, AND T. G. SPIRO, *J. Chem. Phys.* **64**, 2159 (1976).
32. B. CHASE, *Analytical Chem.* **59**, 881A (1987).